

From Octopus to Dendrite - Semiflexible Polyelectrolyte Brush Condensates in Trivalent Counterion Solution

Lei Liu¹ and Changbong Hyeon^{1, a)}

Korea Institute for Advanced Study, Seoul 02455, Republic of Korea

(Dated: 5 April 2024)

Interplay between counterion-mediated interaction and stiffness inherent to polymer chain can bring substantial complexity to the morphology and dynamics of polyelectrolyte brush condensates. Trivalent counterions induce collapse of flexible polyelectrolyte brushes, over a certain range of grafting density, into octopus-like surface micelles; however, if individual chains are rigid enough, the ion-mediated local nematic ordering assembles the brush chains into fractal-like dendritic condensates whose relaxation dynamics is significantly slower than that in the surface micelles. Notably, the trivalent ions condensed in the dendritic condensates are highly mobile displaying quasi-one-dimensional diffusion in parallel along the dendritic branches. Our findings in this study are potentially of great significance to understanding the response of cellular organization such as chromosomes and charged polysaccharides on membranes to the change in ionic environment.

I. INTRODUCTION

Responses of polyelectrolytes (PEs) to the changes in ionic environment and chain stiffness have been extensively studied in polymer sciences^{1–5}. However, new discoveries on the properties of PE are still being made through studies on biopolymers^{6–9}. Also under active investigation are the effects of other variables and constraints on the higher order organization and dynamics of PE found in biological systems^{10–12}.

Demonstrated in both experiments and computational studies^{13–19}, even the conformational adaptation of a single PE chain can be highly complex. Whereas flexible PE chains form compact globules in the presence of counterions⁵, the same condition drives semiflexible PE chains (e.g., dsDNA) to toroidal conformations or metastable rod-like bundles comprised of varying number of racquet structures. Geometrical constraints such as confinement^{20,21} and increasing density of PE could add another level of complexity to the system. For example, DNA chain in a viral capsid or nuclear envelope adopts a densely packed structure with the swelling due to the volume exclusion being suppressed by the confinement and counterions^{12,22–24}. Further, statistically distinct conformations of DNA emerge depending on the amount and type of counterions being added^{25,26}.

PE brush^{27,28}, a spatial organization with one end of many PE chains densely grafted to 2D surface, is another system of interest to be studied. In particular, the novel functions and adaptability discovered in biopolymer brush²⁹ deserve much attention. For example, brush layer of hyaluronic acid, a negatively charged flexible polysaccharide molecule serving as a main component of the extracellular matrix³⁰, modulates the interaction between cells and their environment³¹. The brush of Ki-67, a disordered protein bearing a large positive net charge, found on the surface of mitotic chromosomes prevents

aggregation of chromosomes³².

Morphology of a polymer brush condensed in poor solvent has been studied by using theories and simulations for decades^{33–41}. Depending on the chain stiffness, brush condensates adopt diverse morphological patterns that vary from semi-spherical octopus-like micelle domains to cylindrical bundles of rigid chains which protrude from the grafting surface. It was shown that when the grafting density is in a proper range, multivalent counterions can collapse flexible PE brush even in *good* solvent into octopus-like surface micelles displaying substantial lateral heterogeneity^{42–44}, which has recently been confirmed experimentally for polystyrene sulfonate brush condensates in $Y(NO_3)_3$ solution⁴⁵.

However, we note that the aforementioned studies on the formation of surface micelles from ion-induced collapse of PE brush are still at odds with the findings by Bracha *et al.*⁴⁶ which reported fractal-like dendrite domains as a result of multivalent counterion (Spd^{3+}) induced collapse of DNA brush. Although the previous studies on flexible PE brush^{42–44} captured a number of essential features reported by Bracha *et al.*⁴⁶, qualitative difference in the morphology of brush condensate still exists, thus requiring further investigation. To our knowledge, PE brush condensates with dendritic morphology remain unexplored both in theory and computation. To this end, we extended our former work⁴³ to scrutinize the effect of semiflexibility of PE chain on the brush morphology and dynamics in trivalent counterion solution.

In this study, we adapted a well tested coarse-grained model of strong polyelectrolyte PE brush^{43,47–49}. As shown in Fig. 1A, total $M(= 16 \times 16)$ PE chains were grafted to the triangular lattice on uncharged surface. Each PE chain consists of $N(= 80)$ negatively charged monomers and a neutral terminal monomer grafted to the surface. The lattice spacing was selected to ensure the lateral overlap between neighboring chains. The rigidity of PE chains was adjusted by varying the bending rigidity parameter κ . We added trivalent salts to the pre-equilibrated PE brush in salt-free condition, and induced the collapse into brush condensate. Details of the model

^{a)}hyeoncb@kias.re.kr

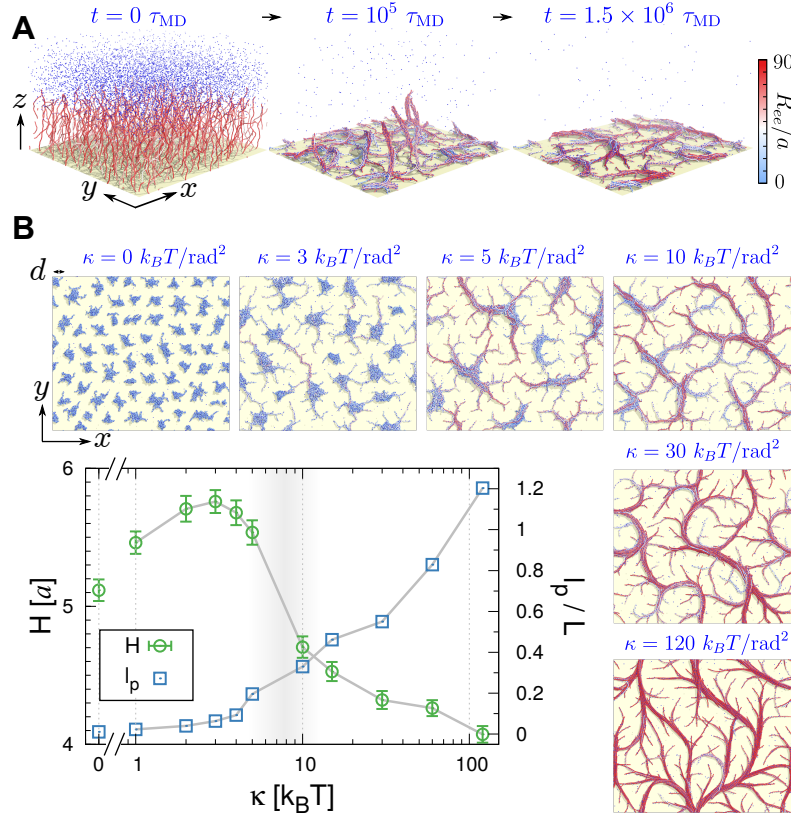


FIG. 1. Model and morphologies of the brush condensates at varying chain stiffness. (A) The polyelectrolyte brush was modeled by 16×16 polymer chains, each carrying $N = 80$ negatively charged monomers, grafted in a triangular lattice of spacings $d = 16a$ on the surface at $z = 0$. In the presence of trivalent cations (blue dots), a pre-equilibrated brush forms multiple bundles, and eventually fully collapses onto the surface. For the sake of visual clarity, monovalent cations released from the chains, as well as monovalent anions added with trivalent cations, are not shown. Individual chains are color-coded from blue to red based on their end-to-end distance R_{ee} . (B) Brush height H and apparent persistence length l_p of chains in the brush (see **Model and Methods**) normalized by $L(= Na)$ at different κ (main panel). Six snapshots of brush condensates obtained from simulations performed with different κ are depicted in the smaller panels.

and simulation methods are given in **Model and Methods**. The results of this work are organized such that we first address the overall morphology of brush condensate under 1:3 stoichiometric condition of trivalent counterion with respect to a monovalent charge on each monomer. Next, the local structure of brush chain is characterized by exploiting the liquid crystal order parameters. Finally, we investigate the dynamics of brush condensates and of condensed counterion at varying κ by calculating the intermediate scattering function.

II. RESULTS

Morphology of brush condensates. Regardless of the value of κ , the PE brush fully collapses onto the grafting surface due to the osmotic pressure of ions, which differs from neutral semiflexible polymer brushes or salt-free PE brushes in poor solvent where the aggregated bundles protrude out of the grafting surface^{38,40,50}. The morphology of the condensate depends critically on κ (Fig. 1B).

(i) For small κ ($\lesssim 3 k_B T / \text{rad}^2$, $l_p < L/10$), the PE brush forms octopus-like surface micelle domains demarcated by the chain-depleted grain boundaries. The average height of the brush H increases with κ ($\leq 3 k_B T / \text{rad}^2$). So does the surface area of the domain projected onto the xy -plane (see also Fig. S1). (ii) For large κ ($> 15 k_B T / \text{rad}^2$, $l_p > L/2$), the condensed chains are organized into a dendritic assembly. Neighboring chains are assembled together, forming axially coaligned branches of varying thickness. The density of chain monomer slightly increases as the chain gets stiffer (see Fig. S2A), which reduces brush height. It is also noted that the end-to-end distance R_{ee} of the collapsed polymers, color-coded from blue to red for individual chains, displays the broadest distribution at an intermediate stiffness $3 < \kappa < 15 k_B T / \text{rad}^2$, which indicates that the conformational ensemble displays the most heterogeneous distribution in this range of κ (see also Fig. S3A,B).

To quantify the in-plane lateral configuration of the

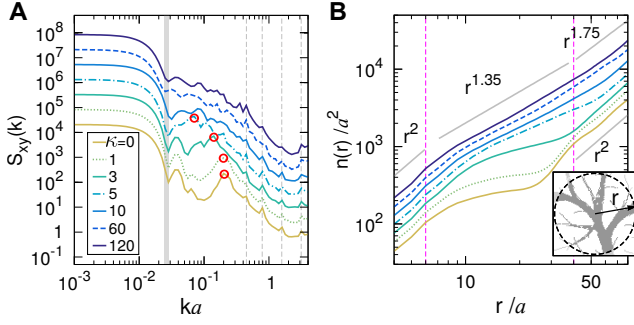


FIG. 2. Structure of brush condensates. (A) In-plane static structure factor $S_{xy}(k)$ as a function of wave number k for brushes of different κ . The gray solid bar demarcates the range $2\pi/L_x \leq k \leq 2\pi/L_y$, i.e., the periodic boundary of the simulation box. The red circles highlight the position of primary peak when $\kappa \leq 5 k_B T/\text{rad}^2$. (B) Area of the condensate on $z = 0$ plane $n(r)$, as a function of a linear dimension r with respect to its center. One exemplary illustration is provided in the inset. For visual clarity, the curves in (A,B) are shifted upward progressively.

brush, we calculated the 2D static structure factor

$$S_{xy}(k) = \left\langle \left\langle \frac{1}{N_m} \left| \sum_{i,j=1}^{N_m} e^{i\vec{k} \cdot (\vec{r}_i - \vec{r}_j)} \right| \right\rangle_{|\vec{k}|} \right\rangle, \quad (1)$$

where $N_m = M \times N$ is the total number of non-grafted chain monomers, \vec{r}_i is the position of the i -th monomer, and \vec{k} is a 2D wave vector in the xy plane. $S_{xy}(k)$ is evaluated by first integrating over the space of $|\vec{k}| = k$, followed by averaging over the ensemble of MD trajectories. $S_{xy}(k)$ exhibits distinct profiles when κ is varied (Fig. 2A). For octopus-like micelles, there is a primary peak (indicated by red circles) characterizing the size (area) of the domain, whose position shifts to a smaller wave number as κ increases, indicating that the domain size grows with κ . However, this peak gradually vanishes as the stiffness of chain is increased. The absence of the peak in $S_{xy}(k)$ is due to the morphological transition from the finite-sized surface micelles to the scale-free dendritic assembly.

To quantify the dendritic patterns in 2D, we further analyzed their fractal dimensions \mathcal{D}_f . We divide the grafting surface into square lattices with each cell size of $a \times a$. When at least one chain monomer is present in a cell, the cell contributes to the “area” of the condensate. The area of dendritic pattern within a radius r is $n(r) = \langle a^2 \sum_{p,q} o_{p,q} \Theta(r - r_{p,q}) \rangle$, where $\Theta(\dots)$ is the Heaviside step function, $o_{p,q} = \Theta[\sum_{i=1}^{N_m} \delta(x_i - pa)] \times \Theta[\sum_{i=1}^{N_m} \delta(y_i - qa)]$, and $r_{p,q}$ is the distance of the cell from a center of high monomer density. $n(r)$ was obtained by averaging over the cells with the five highest monomer density in each snapshot.

$n(r)$ scales as $n(r) \sim r^{\mathcal{D}_f}$, and the value of the scaling exponent \mathcal{D}_f varies at different length scale (Fig. 2B). (i) In the range of $6 < r/a < 40$, $\mathcal{D}_f \approx 1.35$ for brushes of

rigid chains, whereas $\mathcal{D}_f \approx 0$ for flexible brushes. The transition from micelle domain with finite size ($\mathcal{D}_f \approx 0$) to scale-free dendritic assembly ($\mathcal{D}_f > 0$) is observed at $\kappa \approx 5 k_B T/\text{rad}^2$ (see Fig. 1B). (ii) At $r/a > 50$, $\mathcal{D}_f \approx 1.75$ for rigid brushes ($\kappa > 15 k_B T/\text{rad}^2$), and $\mathcal{D}_f \approx 2$ for flexible brushes ($\kappa \leq 5 k_B T/\text{rad}^2$). The scaling exponent $\mathcal{D}_f \approx 2$ arises when the monomer is uniformly distributed on the surface such that the density of condensates $\rho_m = n(r)/\pi r^2$ is constant with respect to r . Unlike the octopus-like micelles surrounded by the chain-depleted zone, the dendritic condensate percolates over the entire surface. Analyzing fluorescence images of dendritic condensate of dsDNA brush through a similar method⁴⁶, Bracha *et al.* reported $\mathcal{D}_f = 1.75$.

Another quantity often being used to address the fractality is the 2D version of radial distribution function, defined as $C_{xy}(r) = \sum_{i>j} \delta(r_{i,j} - r)/\pi r^2 N_m$. C_{xy} scales as $r^{\mathcal{D}_f-2}$ in a fractal aggregate of dimension \mathcal{D}_f ^{51–53}. Consistent with the analysis of $n(r)$, C_{xy} of chain monomers indeed follows a scaling $C_{xy} \sim r^{1.35-2} = r^{-0.65}$ in the intermediate range of r when κ is large (Fig. S4C).

Local chain organization. The local structure of chains in the brush condensates also changes with κ (see the insets of Fig. 3A). When chains are flexible, the adjacent chains condensed to the same micelle appear highly entangled. It is not visually clear whether two monomers close in space are in the same chain or in different chains. In contrast, when chains are rigid, they are parallelly aligned, and the strong orientational correlation between consecutive bonds allows us to easily discern one chain from another. To characterize the local ordering of polymer segments in the collapsed brush, we employed the liquid crystal order parameter^{54,55}. For any two consecutive monomers $i, i+1$ in the same chain, a unit bond vector \vec{b}_i is defined by its orientation $\vec{u}_i = (\vec{r}_{i+1} - \vec{r}_i)/|\vec{r}_{i+1} - \vec{r}_i|$, and its position $\vec{v}_i = (\vec{r}_{i+1} + \vec{r}_i)/2$. The radial distribution of such two bond vectors can be evaluated as

$$g_0^b(r_\perp, r_\parallel) = \frac{\sum_{i,j} \delta(r_{ij,\perp} - r_\perp) \delta(r_{ij,\parallel} - r_\parallel)}{\pi r_\perp^2 r_\parallel N_b}, \quad (2)$$

where $\vec{r}_{ij}^b = \vec{v}_j - \vec{v}_i$, $\vec{r}_{ij,\parallel} = \vec{r}_{ij}^b \cdot \vec{u}_i^b$, $\vec{r}_{ij,\perp} = \vec{r}_{ij}^b - \vec{r}_{ij,\parallel}$, and $N_b = M \times N$ is the total number of bonds in the brush. The vector \vec{r}_{ij}^b , pointing from bond \hat{b}_i to another bond \hat{b}_j , was decomposed into the parallel and perpendicular components ($\vec{r}_{ij,\parallel}$ and $\vec{r}_{ij,\perp}$) with respect to the orientation of \hat{b}_i . The heat map of $g_0^b(r_\perp, r_\parallel)$ in Fig. 3A, indicates that the bonds of flexible chains in a micelle are isotropically distributed. As κ increases, density correlation first rises along the axis of r_\parallel . Because the effective attraction between monomers from neighboring chains increases with κ (Fig. S4B), bond density correlation also appears on the r_\perp axis when $\kappa > 10 k_B T/\text{rad}^2$.

The relative orientational correlation between bond vectors, which cannot be described by $g_0^b(r_\perp, r_\parallel)$ alone,

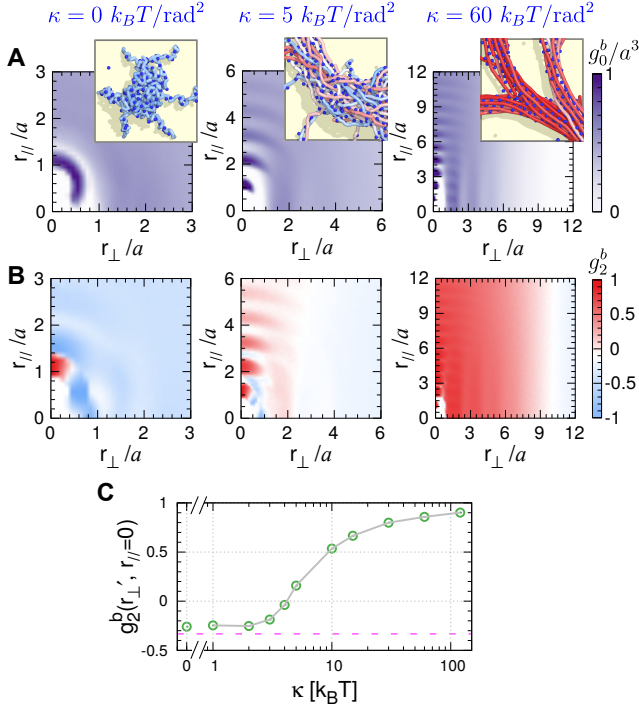


FIG. 3. Local chain organizations. (A) Heat map of the density distribution of bonds g_0^b (Eq.2), and (B) orientation order parameter g_2^b (Eq.3) as a function of r_\perp and r_\parallel . From left to right panels, $\kappa = 0, 5, 60 \text{ k}_B T / \text{rad}^2$, respectively. Insets are snapshots of a small region, with a size of $32a \times 32a$, in the corresponding brush condensates. (C) Inter-chain bond orientational order $g_2^b(r_\perp^*, 0)$ as a function of κ , where r_\perp^* is the position of the highest peak in $g_0^b(r_\perp, 0)$.

is quantified by calculating^{54,55}

$$g_2^b(r_\perp, r_\parallel) = \frac{\sum_{i,j} \cos(2\theta_{ij}) \delta(r_{ij,\perp} - r_\perp) \delta(r_{ij,\parallel} - r_\parallel)}{\sum_{i,j} \delta(r_{ij,\perp} - r_\perp) \delta(r_{ij,\parallel} - r_\parallel)}, \quad (3)$$

where θ_{ij} is the angle between \hat{b}_i and \hat{b}_j , thus $\cos(2\theta_{ij}) = (\vec{u}_i \cdot \vec{u}_j)^2 - 1$. $\cos(2\theta) \leq 0$ if $\pi/4 \leq \theta \leq 3\pi/4$. In the case of an isotropic distribution, $g_2^{b*} = \int_0^\pi \sin(\theta) \cos(2\theta) d\theta / \int_0^\pi \sin(\theta) d\theta = -1/3$. For flexible chains with $\kappa = 0 \text{ k}_B T / \text{rad}^2$ (Fig. 3B left), the positive correlation arises only from their nearest neighboring bond along the chain, and g_2^b converges to $-1/3$ within a very short range ($r < 2a$). At $\kappa = 5 \text{ k}_B T / \text{rad}^2$, intra-chain bonds are well ordered, but on the r_\perp axis $g_2^b \approx -1/3$ when $r_\perp > 2.5a$, which suggests that except for the nearest neighbors, the bonds from different chains are still poorly aligned. Lastly, at $\kappa = 60 \text{ k}_B T / \text{rad}^2$, $g_2^b(r_\perp, r_\parallel) > 0$ in both r_\perp and r_\parallel directions with $r_\perp, r_\parallel \gg 1$, in agreement with the observation that rigid chains are bundled together forming the branches of the condensate.

To highlight the effect of κ on the local *inter-chain* organization in the condensate, we plotted $g_2^b(r_\perp^*, 0)$ (Fig. 3C) against κ , by considering it as a single-valued

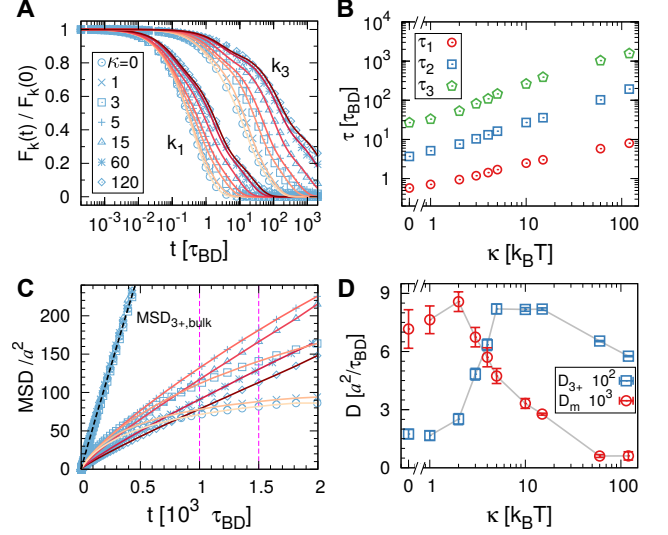


FIG. 4. Dynamic properties of brush condensate and counterions. (A) Normalized intermediate scattering function $f_{xy}(k, t) = F_{xy}(k, t) / F_{xy}(k, 0)$ (Eq.4) of chain monomers at wave numbers $2\pi/k_1 = 1.1/a$ and $2\pi/k_3 = 3.6/a$. (B) Conformational relaxation time of chains $\tau_i = \int f_{xy}(k_i, t) dt$ with different κ . (C) Mean square displacement of trivalent cations, either trapped in the condensate or free in the bulk. Symbols have the same meanings as in (A). (D) Diffusion coefficients of trapped trivalent cations (3+) and chain monomers.

estimate of the inter-chain bond alignment, where r_\perp^* is position of the highest peak of $g_0^b(r_\perp, 0)$ (see also Fig. S5). In the brush condensate, chains are randomly entangled with each other when $\kappa \leq 3 \text{ k}_B T / \text{rad}^2$, but they display nearly perfect alignment when $\kappa > 30 \text{ k}_B T / \text{rad}^2$. This disorder-to-order “transition” takes place around $\kappa \approx 5 \text{ k}_B T / \text{rad}^2$ (Fig. 3C).

Dynamics of brush condensates. In order to quantify the dynamics of PE brush, we calculated the intermediate scattering function, which is the density-density time correlation function (van Hove correlation function) in Fourier domain,

$$F_{xy}(k, t) = \left\langle \left\langle \frac{1}{N_m} \sum_{m=1}^{N_m} e^{i\vec{k} \cdot \vec{r}_m(t+t_0)} \sum_{n=1}^{N_m} e^{-i\vec{k} \cdot \vec{r}_n(t_0)} \right\rangle_{|\vec{k}|} \right\rangle_{t_0} \quad (4)$$

where $\langle \langle \dots \rangle_{|\vec{k}|} \rangle_{t_0}$ is an average over time t_0 and over the direction of a 2D wave vector \vec{k} of magnitude k . The dynamics of brush chain at different length scales can be probed in terms of $F_{xy}(k, t)$ evaluated at different k ($k_i = 2\pi/r_i^*$ where $i = 1, 2, 3$ and $r_i^*/a = 1.1, 2.0, 3.6$ are the positions of the three highest peaks in the radial distribution function of chain monomers (see Fig. S4C,D)). The normalized function $f_{xy}(k, t) = F_{xy}(k, t) / F_{xy}(k, 0)$, with k_1 and k_3 , are shown in Fig. 4A, and the corresponding mean relaxation time $\tau_i = \int_0^\infty f_{xy}(k_i, t) dt$ is presented in Fig. 4B. At a small length scale k_1^{-1} ,

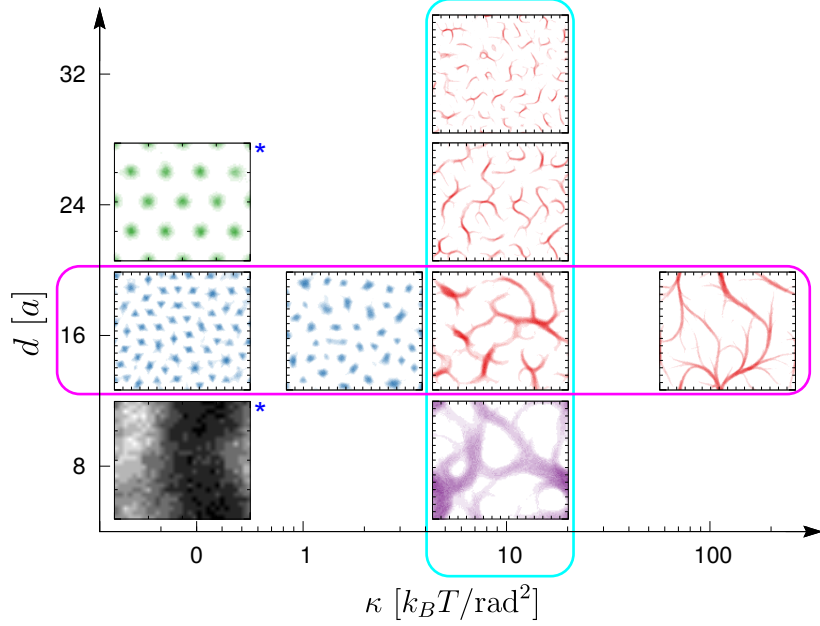


FIG. 5. Time-averaged monomer density heat maps of PE brush condensates as a function of the bending rigidity parameter κ and the grafting distance d . Visually distinct morphologies are colored differently: homogeneous compact layer (black), octopus-like surface micelles (blue), single-chain tadpole-like condensate (green), dendritic domains and networks (red and purple). Those labeled with asterisks (*) depict the simulation results of a smaller brush ($M = 4 \times 4$) from our previous study⁴³.

$f_{xy}(k_1, t)$ decays to zero within the timescale of $t < 10\tau_{BD}$, which implies that chain monomers are fluidic beyond this time scale. But, compared to octopus-like micelle with $\kappa = 0 \text{ } k_B T / \text{rad}^2$, the dendritic assembly made of brush chains with $\kappa = 120 \text{ } k_B T / \text{rad}^2$ displays ~ 14 -fold slower relaxation profile of $f_{xy}(t)$. The relaxation becomes much slower at larger length scale k_3^{-1} , and τ_3 for rigid chain comprising the dendritic assembly is as long as our total simulation time ($\sim \mathcal{O}(10^3)\tau_{BD}$). We also notice that the ratio of relaxation times, $\eta_i = \tau_i(\kappa = 120 \text{ } k_B T / \text{rad}^2) / \tau_i(\kappa = 0 \text{ } k_B T / \text{rad}^2)$ at the three position of r_i^* (with $i = 1, 2, 3$) takes an order of $\eta_3 > \eta_2 > \eta_1$. This is expected because the contribution from inter-chain relaxation to the total relaxation time is higher at r_3 than at r_1 . A tight and well aligned chain organization at $\kappa = 120 \text{ } k_B T / \text{rad}^2$ further increases τ_3 in comparison to τ_1 . For the most rigid dendrite, τ_3 is ~ 60 -fold greater than that of the surface micelle formed by flexible PE brush.

Next, the mobility of trivalent cations, either trapped in the condensate (within λ_B from the chains) or free in the bulk solution, were quantified using an ensemble- and time-averaged mean squared displacement, $\text{MSD}(t) = \langle |\vec{r}_i(t+t_0) - \vec{r}_i(t_0)|^2 \rangle_{t_0}$, as shown in Fig. 4C. When $\kappa \leq 5 \text{ } k_B T / \text{rad}^2$, although trapped ions are mobile, MSD shows a long-time subdiffusive behavior because ions are confined in individual micelles⁴⁵ (Supplementary Movie 1). By contrast, for $\kappa > 10 \text{ } k_B T / \text{rad}^2$, condensed ions can freely diffuse along the dendritic branches. As a result, MSD grows linearly with time.

The diffusion coefficient of trapped trivalent cation, estimated using $D = \text{MSD}(t) / 6\Delta t$ for $\Delta t = 1 \times 10^3$ to $1.5 \times 10^3 \tau_{BD}$, is non-monotonic with κ . This change agrees with the change of the brush morphology where ions are confined. In the micelle phase, micelle size grows with κ , which provides larger space for the trapped ions to navigate. In the dendrite phase, the effective attraction between neighboring chains, mediated by the counterions, increases with κ (see Figs. S2A, S4B) and tightens the bundling of PE, which in turn reduces the mobility of the condensed ions. The trapped trivalent ions diffuse > 10 -fold slower than those in the bulk, but still ~ 100 -fold faster than chain monomers in the dendritic assembly, even though the same value of bare diffusion coefficient was assumed for all ions and chain monomers. The bundles of rigid chains form a network of “highway”, on which the condensed trivalent ions freely diffuse (Supplementary Movie 2).

III. DISCUSSION

Effect of grafting density on the morphology of brush condensates. The morphological transitions from the octopus-like surface micelles to the dendritic condensates are reminiscent of sol-to-gel transition. Analogous to gelation transition, the “bond probability” p can be tuned by changing either the chain stiffness (κ) or grafting distance (d). Below the gelation point ($p < p_c$) isolated domains are observed; and above the

gelation point ($p > p_c$) the domains are all connected together, covering the entire space. We further performed simulations of a semiflexible brush, at $\kappa = 10 k_B T / \text{rad}^2$, by varying the inter-chain spacing d (see Fig. 5 and Fig. S6). Time-averaged monomer density heat maps of PE brushes $\langle \rho(x, y) \rangle$ (Fig. 5) visualize how the morphology of brush condensates changes as a function of the chain bending rigidity parameter κ and the inter-chain spacing d .

Notably, changes in κ and d display qualitatively different effects on the morphologies below and above the “gelation point.” At $d = 16a$ with increasing κ (panels enclosed by the magenta boundary in Fig. 5), the initially sol-like micelles domain are percolated into gel-like dendritic pattern whose branches span the entire surface. In contrast, when the chain stiffness is fixed to $\kappa = 10 k_B T / \text{rad}^2$ and grafting distance is varied from a large value ($d = 32a$) to a small one ($d = 8a$) (panels enclosed by the cyan boundary in Fig. 5), the initial sol-like isolated domains are characterized by the heterogeneous condensates made of semiflexible chains, collapsed into toroids or rod-like bundles on site, not by the tadpole or octopus-like micelle condensates; and with decreasing d the chains collapse and further assemble into a dendritic pattern and a non-uniform fractal-like meshwork layer.

Size of octopus-like surface micelle. For octopus-like surface micelle, a scaling argument is developed based on equilibrium thermodynamics⁴³. The domain size is determined by the balance between the surface tension resulting from the counterion-mediated attraction and the elastic penalty to stretch the grafted chains to form a surface micelle. When $\kappa \leq 3 k_B T / \text{rad}^2$, l_p is small enough to approximate the individual PE as a flexible chain with Kuhn length $2l_p$. For an octopus-like domain containing n chains within a surface area $\sim R_c^2 \simeq l_p^2 (nN/l_p)^{2\nu}$, the surface energy is $F_{n,\text{surf}} = \xi k_B T l_p^2 (nNa/l_p)^{2\nu}$, where ξ sets the scale of attraction between chain segments and ν is the Flory exponent. Meanwhile, the elastic penalty is $F_{n,\text{el}} = nk_B T R_c^2 / l_p^2 N_s = nk_B T R_c / l_p = k_B T \sigma R_c^3 / l_p$, where $N_s = R_c / l_p$ is the number of statistical segments in each chain to be stretched to reach the micelle, and $\sigma = n / R_c^2$ is the chain grafting density. The total free energy per area in the octopus-like condensate with n arms is

$$\begin{aligned} \frac{f_{\text{octo}}}{k_B T} &= \frac{1}{k_B T} \frac{F_{n,\text{surf}} + F_{n,\text{el}}}{R_c^2} \\ &= \frac{\xi(\sigma N a)^{2\nu} l_p^{2-2\nu}}{R_c^{2-4\nu}} + \frac{\sigma R_c}{l_p}. \end{aligned} \quad (5)$$

Minimization of f_{octo} with respect to R_c provides the micelle size corresponding to a minimum free energy $R_c^* \sim l_p^{\frac{3-2\nu}{3-4\nu}} (Na)^{\frac{2\nu}{3-4\nu}} \sigma^{\frac{2\nu-1}{3-4\nu}}$. For $\nu = 1/3$, R_c^* increases as $\sim l_p^{7/5}$ (thus with κ), until neighboring micelles is about to overlap. Beyond this overlap point, the

picture of isolated semispherical micelles no longer holds.

Fractal dimension of dendritic condensate. In the case of dendritic condensate, we found that $n(r) \sim r^{\mathcal{D}_f}$. In particular, $\mathcal{D}_f \approx 1.75$, observed at large r ($r/a > 50$) was also reported in Bracha *et al.*'s experiment⁴⁶. Incidentally, the morphology of aggregate changes depending on how trivalent salt is added⁴⁶. Thus, the formation of dendritic morphologies are effectively made under kinetic gelation rather than equilibrium one.

The premise that the process of dendritic assembly is kinetically controlled guides the direction of our theoretical analysis. Since the collapse is effectively irreversible and the bundles grow preferentially from the “active front” of the preexisting domain⁵⁶, we use the principle underlying the diffusion-limited aggregation⁵⁷ (DLA) to explain the observed fractal dimension. DLA describes a far-from-equilibrium growth phenomenon, where each particle diffuse with a fractal dimension d_w until it binds irreversibly to any particles of the aggregate. A generalized Honda-Toyoki-Matsushita mean-field approximation^{58,59} suggests that, the fractal dimension of the aggregate is

$$\mathcal{D}_{\text{MF}} = \frac{d_s^2 + \eta(d_w - 1)}{d_s + \eta(d_w - 1)}, \quad (6)$$

where in the presence of long-range attractive interactions the probability of growth at a certain position is assumed to be proportional to the gradient of a scalar field (e.g. monomer density) as $\sim |\nabla \phi|^\eta$. For DLA ($\eta = 1$, $d_w = 2$) in 2 dimension ($d_s = 2$), Eq. 6 gives $\mathcal{D}_{\text{MF}} = \mathcal{D}_{f,\text{DLA}} = 5/3$. Numerical simulations report $\mathcal{D}_{f,\text{DLA}} = 1.71^{52,53}$.

DLA has also been exploited to explain the dynamics and aggregation of a 3D gel-like network formed by rigid PE chains in a poor solvent⁶⁰. The fractal nature of the dendritic pattern may well be an outcome of premature quenching of brush configuration to condensates during the competition between the gain in energy upon aggregation and the entropic gain of chain fluctuations.

IV. CONCLUDING REMARKS

Collapse of the brush condensate into either surface micelles⁴⁵ or a dendritic pattern⁴⁶ is controlled by the chain flexibility. Fundamental differences are found in the the dynamics of chains and condensed ions as well as in the microscopic chain arrangement. The new insights into the link between the micro-scale details and brush morphology will be of great use to design material properties and understand biological functions of PE brushes.

V. MODEL AND METHODS

Model and energy potential. As in our previous study⁴³, we used a well tested coarse-grained model of strong polyelectrolyte (PE) brush^{47–49}. Total $M(= 16 \times 16)$ polymer chains were grafted to the uncharged surface of a 2D triangular lattice (Fig. 1A). The lattice spacing d was set to $16a$, which is small enough to ensure the lateral overlap between neighboring chains, where a is the diameter of chain monomers and ions. Each chain consists of $N(= 80)$ negatively charged monomers and a neutral terminal monomer grafted to the surface. The simulation box has a dimension of $L_x \times L_y \times L_z = (\sqrt{M}d) \times (\sqrt{3M}d/2) \times (2Na) = 256a \times 128\sqrt{3}a \times 160a$. Periodic boundary conditions were applied along the x and y axes, and impenetrable neutral walls were placed at $z = 0$ and $2Na$.

We considered the following energy potentials to model a semiflexible PE brush in *good* solvents with multivalent salts. First, the distance between the neighboring chain monomers was constrained by a finite extensible nonlinear elastic bond potential

$$U_{bond}(r) = -\frac{k_0 R_0^2}{2} \log \left(1 - \frac{r^2}{R_0^2} \right), \quad (7)$$

with a spring constant $k_0 = 5.83 k_B T / a^2$ and a maximum extensible bond length $R_0 = 2a$. Second, the chain stiffness was modulated with an angular potential

$$U_{angle}(\theta) = \kappa(\theta - \pi)^2, \quad (8)$$

where κ is the bending rigidity parameter and θ is the angle between three consecutive monomers along the chain. Third, the excluded volume interaction was modeled in between ions and chain monomers by using the Weeks-Chandler-Andersen potential

$$U_{excl}(r) = 4\epsilon \left[\left(\frac{a}{r} \right)^{12} - \left(\frac{a}{r} \right)^6 + \frac{1}{4} \right] \Theta(2^{1/6}a - r), \quad (9)$$

in which $\epsilon = 1 k_B T$ and $\Theta(\dots)$ denotes a Heaviside step function. Fourth, the Coulombic interactions were assigned between charged particles i, j , which include both chain monomers and ions,

$$U_{elec}(r) = \frac{k_B T \lambda_B z_i z_j}{r}, \quad (10)$$

where $z_{i,j}$ is the valence of charge. The Bjerrum length is defined as $\lambda_B = e^2 / (4\pi\epsilon_0\epsilon_r k_B T)$, where ϵ_0 is the vacuum permittivity and ϵ_r is the relative dielectric constant of the solvent. Lastly, the confinement of the wall was considered to repel any monomer, that approaches the wall closer than $a/2$ such that

$$U_{wall}(z) = 4\epsilon \left[\left(\frac{a}{z + \Delta} \right)^{12} - \left(\frac{a}{z + \Delta} \right)^6 + \frac{1}{4} \right] \Theta(a/2 - z), \quad (11)$$

with $\Delta = (2^{1/6} - 1/2)a$. For simplicity, we assume the same diameter a for all the ions and chain monomers. For dsDNA, the mean bond length $\langle b \rangle = 1.1a$ ($\approx a$) in our model maps to the effective charge separation (≈ 1.7 Å) along the chain. Considering $\lambda_B = 7.1$ Å in water at room temperature, we set $\lambda_B = 4a$ ($\approx 7.1/1.7 \times a$). Since the focus of this study is on the effects of the bending rigidity of PE chain, κ in Eq.8 was adjusted in the range, $0 \leq \kappa \leq 120 k_B T / \text{rad}^2$.

Simulation. For conformational sampling of the brush, we integrated the Langevin equation at under-damped condition⁶¹,

$$m \frac{d^2 \vec{r}_i}{dt^2} = -\zeta_{MD} \frac{d\vec{r}_i}{dt} - \vec{\nabla}_{\vec{r}_i} U(\vec{r}_1, \vec{r}_2, \dots) + \vec{\xi}(t), \quad (12)$$

using a small friction coefficient $\zeta_{MD} = 0.1m/\tau_{MD}$ and a time step $\delta t = 0.01\tau_{MD}$, with the characteristic time scale $\tau_{MD} = (ma^2/\epsilon)^{1/2}$. We started from an initial configuration where polymer chains were vertically stretched, and monovalent counterions were homogeneously distributed in the brush region. This salt-free brush was first equilibrated for the time of $10^4 \tau_{MD}$, then trivalent cations at a 1:3 stoichiometric concentration ratio with respect to the polyelectrolyte charges⁴³ were randomly added together with its monovalent coions (anions) into the brush-free zone (see Fig. 1A). Depending on the value of κ , trivalent cations induce an immediate collapse or bundling of neighboring chains in the brush. In the latter case, an intermediate bundle either merges into a thicker one with other bundles nearby, or collapses onto the grafting surface *irreversibly*. For stiff chains with $\kappa = 60$ or $120 k_B T / \text{rad}^2$, it takes longer than $10^6 \tau_{MD}$ before the whole brush collapses and the mean height of chains reaches the steady state. Production runs were generated further for $5 \times 10^4 \tau_{MD}$. Brush configurations were collected every $50\tau_{MD}$ for the analysis of static properties. Unless stated otherwise, all the conformational properties reported here were averaged over the ensemble of trajectories.

To probe the dynamics of condensates, we performed Brownian dynamics (BD) simulations by integrating the following equation of motion

$$\frac{d\vec{r}_i}{dt} = -\frac{D_{i0}}{k_B T} \vec{\nabla}_{\vec{r}_i} U(\vec{r}_1, \dots, \vec{r}_N) + \vec{R}_i(t), \quad (13)$$

where D_{i0} is the bare diffusion coefficient of the i -th particle, and $\vec{R}_i(t)$ is the Gaussian noise satisfying $\langle \vec{R}_i(t) \rangle = 0$ and $\langle \vec{R}_i(t) \cdot \vec{R}_j(t') \rangle = 6D_{i0}\delta_{ij}\delta(t - t')$. D_{i0} was estimated via $k_B T / 6\pi\eta R$, where $\eta = 0.89 \times 10^3$ Pa·s is the viscosity of water and R is the hydration radius of all the particles. We chose an integration time step $\delta t_{BD} = 2 \times 10^{-4} \tau_{BD}$ with the Brownian time $\tau_{BD} = a^2 / D_{i0}$ (~ 4 ns, assuming that $R \sim 10$ Å). Starting from the last configuration of brush in MD simulations, the BD simulation was performed for $4 \times 10^3 \tau_{BD}$. Simulations were all carried out by using

ESPResSo 3.3.1 package^{62,63}. More details can be found in Ref.⁴³.

Apparent persistence length of brush chain. By using a simplifying assumption that as an isolated semiflexible chain the correlation between bond vectors exponentially decays with their separation along the chain ($g(s) = \langle \vec{u}_i \cdot \vec{u}_{i+s} \rangle \sim e^{-s/l_p}$, where $\vec{u}_i = (\vec{r}_{i+1} - \vec{r}_i)/|\vec{r}_{i+1} - \vec{r}_i|$) (Fig. S7), we quantified an “apparent” persistent length l_p .

VI. SUPPLEMENTARY MATERIAL

Supplementary material contains the Supplementary Figures S1 – S7 and Supplementary Movies 1 and 2.

ACKNOWLEDGMENTS

We thank the Center for Advanced Computation in KIAS for providing computing resources.

- ¹F. Oosawa, *Polyelectrolytes* (Marcel Dekker, Inc., 1971).
- ²J. Skolnick and M. Fixman, “Electrostatic persistence length of a wormlike polyelectrolyte,” *Macromolecules* **10**, 944–948 (1977).
- ³J. L. Barrat and J. F. Joanny, “Persistence length of polyelectrolyte chains,” *Europhys. Lett.* **24**, 333 (1993).
- ⁴B.-Y. Ha and D. Thirumalai, “Electrostatic persistence length of a polyelectrolyte chain,” *Macromolecules* **28**, 577–581 (1995).
- ⁵H. Schiessel, “Counterion condensation on flexible polyelectrolytes: dependence on ionic strength and chain concentration,” *Macromolecules* **32**, 5673–5680 (1999).
- ⁶G. Caliskan, C. Hyeon, U. Perez-Salas, R. M. Briber, S. A. Woodson, and D. Thirumalai, “Persistence Length Changes Dramatically as RNA Folds,” *Phys. Rev. Lett.* **95**, 268303 (2005).
- ⁷S. Moghaddam, G. Caliskan, S. Chauhan, C. Hyeon, R. Briber, D. Thirumalai, and S. Woodson, “Metal ion dependence of cooperative collapse transitions in RNA,” *J. Mol. Biol.* **393**, 753–764 (2009).
- ⁸L. Liu and C. Hyeon, “Contact statistics highlight distinct organizing principles of proteins and rna,” *Biophys. J.* **110**, 2320–2327 (2016).
- ⁹M. Emanuel, N. H. Radja, A. Henriksson, and H. Schiessel, “The physics behind the larger scale organization of DNA in eukaryotes,” *Phys. Biol.* **6**, 025008 (2009).
- ¹⁰D. J. Needleman, M. A. Ojeda-Lopez, U. Raviv, H. P. Miller, L. Wilson, and C. R. Safinya, “Higher-order assembly of microtubules by counterions: from hexagonal bundles to living necklaces,” *Proc. Natl. Acad. Sci. U. S. A.* **101**, 16099–16103 (2004).
- ¹¹N. V. Hud and I. D. Vilfan, “Toroidal dna condensates: unraveling the fine structure and the role of nucleation in determining size,” *Annu. Rev. Biophys. Biomol. Struct.* **34**, 295–318 (2005).
- ¹²H. Kang, Y.-G. Yoon, D. Thirumalai, and C. Hyeon, “Confinement-induced glassy dynamics in a model for chromosome organization,” *Phys. Rev. Lett.* **115**, 198102 (2015).
- ¹³A. Martin, M. Davies, B. Rackstraw, C. Roberts, S. Stolnik, S. Tendler, and P. Williams, “Observation of DNA-polymer condensate formation in real time at a molecular level,” *FEBS Letters* **480**, 106 – 112 (2000).
- ¹⁴I. D. Vilfan, C. C. Conwell, T. Sarkar, and N. V. Hud, “Time study of DNA condensate morphology: Implications regarding the nucleation, growth, and equilibrium populations of toroids and rods,” *Biochemistry* **45**, 8174–8183 (2006).
- ¹⁵M. J. Stevens, “Simple simulations of DNA condensation,” *Biophys. J.* **80**, 130 – 139 (2001).
- ¹⁶N. Lee and D. Thirumalai, “Dynamics of collapse of flexible polyelectrolytes in poor solvents,” *Macromolecules* **34**, 3446–3457 (2001).
- ¹⁷Z. Ou and M. Muthukumar, “Langevin dynamics of semiflexible polyelectrolytes: Rod-toroid-globule-coil structures and counterion distribution,” *J. Chem. Phys.* **123**, 074905 (2005).
- ¹⁸D. T. Seaton, S. Schnabel, D. P. Landau, and M. Bachmann, “From flexible to stiff: Systematic analysis of structural phases for single semiflexible polymers,” *Phys. Rev. Lett.* **110**, 028103 (2013).
- ¹⁹T. X. Hoang, A. Giacometti, R. Podgornik, N. T. T. Nguyen, J. R. Banavar, and A. Maritan, “From toroidal to rod-like condensates of semiflexible polymers,” *J. Chem. Phys.* **140**, 064902 (2014).
- ²⁰G. Morrison and D. Thirumalai, “Semiflexible chains in confined spaces,” *Phys. Rev. E* **79**, 011924 (2009).
- ²¹A. J. Spakowitz and Z.-G. Wang, “Semiflexible polymer confined to a spherical surface,” *Phys. Rev. Lett.* **91**, 166102 (2003).
- ²²N. V. Hud and K. H. Downing, “Cryo-electron microscopy of λ phage DNA condensates in vitreous ice: The fine structure of DNA toroids,” *Proc. Natl. Acad. Sci. USA* **98**, 14925–14930 (2001).
- ²³A. Leforestier, “Polymorphism of DNA conformation inside the bacteriophage capsid,” *J. Biol. Phys.* **39**, 201–213 (2013).
- ²⁴Z. T. Berendsen, N. Keller, S. Grimes, P. J. Jardine, and D. E. Smith, “Nonequilibrium dynamics and ultraslow relaxation of confined DNA during viral packaging,” *Proc. Natl. Acad. Sci. U. S. A.* **111**, 8345–8350 (2014).
- ²⁵A. Allahverdi, Q. Chen, N. Korolev, and L. Nordenskiöld, “Chromatin compaction under mixed salt conditions: Opposite effects of sodium and potassium ions on nucleosome array folding,” *Sci. Rep.* **5**, 8512 (2015).
- ²⁶J. Yoo, H. Kim, A. Aksimentiev, and T. Ha, “Direct evidence for sequence-dependent attraction between double-stranded dna controlled by methylation,” *Nat. Commun.* **7**, 11045 (2016).
- ²⁷P. Pincus, “Colloid stabilization with grafted polyelectrolytes,” *Macromolecules* **24**, 2912–2919 (1991).
- ²⁸R. Israels, F. A. M. Leermakers, G. J. Fleer, and E. B. Zhulina, “Charged polymeric brushes: Structure and scaling relations,” *Macromolecules* **27**, 3249–3261 (1994).
- ²⁹B. Zappone, M. Ruths, G. W. Greene, G. D. Jay, and J. N. Israelachvili, “Adsorption, lubrication, and wear of lubricin on model surfaces: Polymer brush-like behavior of a glycoprotein,” *Biophys. J.* **92**, 1693–1708 (2007).
- ³⁰S. Attili, O. V. Borisov, and R. P. Richter, “Films of end-grafted hyaluronan are a prototype of a brush of a strongly charged, semiflexible polyelectrolyte with intrinsic excluded volume,” *Biomacromolecules* **13**, 1466–1477 (2012).
- ³¹M. Cohen, D. Joester, B. Geiger, and L. Addadi, “Spatial and temporal sequence of events in cell adhesion: From molecular recognition to focal adhesion assembly,” *ChemBioChem* **5**, 1393–1399 (2004).
- ³²S. Cuylen, C. Blaukopf, A. Z. Politi, T. Müller-Reichert, B. Neumann, I. Poser, J. Ellenberg, A. A. Hyman, and D. W. Gerlich, “Ki-67 acts as a biological surfactant to disperse mitotic chromosomes,” *Nature* **535**, 308–312 (2016).
- ³³P. Lai and K. Binder, “Structure and dynamics of polymer brushes near the θ point: A monte carlo simulation,” *J. Chem. Phys.* **97**, 586–595 (1992).
- ³⁴G. S. Grest and M. Murat, “Structure of grafted polymeric brushes in solvents of varying quality: a molecular dynamics study,” *Macromolecules* **26**, 3108–3117 (1993).
- ³⁵D. R. M. Williams, “Grafted polymers in bad solvents: octopus surface micelles,” *J. Phys. II France* **3**, 1313–1318 (1993).
- ³⁶E. Zhulina, C. Singh, and A. C. Balazs, “Behavior of tethered polyelectrolytes in poor solvents,” *J. Chem. Phys.* **108**, 1175–1183 (1998).
- ³⁷S. K. Pattanayek, T. T. Pham, and G. G. Pereira, “Morphological structures formed by grafted polymers in poor solvents,” *J. Chem. Phys.* **122**, 214908 (2005).

- ³⁸J.-M. Y. Carrillo and A. V. Dobrynin, “Morphologies of planar polyelectrolyte brushes in a poor solvent: Molecular dynamics simulations and scaling analysis,” *Langmuir* **25**, 13158–13168 (2009).
- ³⁹M. Tagliazucchi, M. O. de la Cruz, and I. Szleifer, “Self-organization of grafted polyelectrolyte layers via the coupling of chemical equilibrium and physical interactions,” *Proc. Natl. Acad. Sci. USA* **107**, 5300–5305 (2010).
- ⁴⁰G.-L. He, H. Merlitz, and J.-U. Sommer, “Molecular dynamics simulations of polyelectrolyte brushes under poor solvent conditions: Origins of bundle formation,” *J. Chem. Phys.* **140**, 104911 (2014).
- ⁴¹A. Lappala, S. Mendiratta, and E. M. Terentjev, “Arrested spinodal decomposition in polymer brush collapsing in poor solvent,” *Macromolecules* **48**, 1894–1900 (2015).
- ⁴²B. K. Brettmann, N. Laugel, N. Hoffmann, P. Pincus, and M. Tirrell, “Bridging contributions to polyelectrolyte brush collapse in multivalent salt solutions,” *J. Polym. Sci., Part A: Polym. Chem.* **54**, 284–291 (2016).
- ⁴³L. Liu, P. A. Pincus, and C. Hyeon, “Heterogeneous Morphology and Dynamics of Polyelectrolyte Brush Condensates in Trivalent Counterion Solution,” *Macromolecules* **50**, 1579–1588 (2017).
- ⁴⁴N. E. Jackson, B. K. Brettmann, V. Vishwanath, M. Tirrell, and J. J. de Pablo, “Comparing solvophobic and multivalent induced collapse in polyelectrolyte brushes,” *ACS Macro Letters* **6**, 155–160 (2017).
- ⁴⁵J. Yu, N. E. Jackson, X. Xu, B. K. Brettmann, M. Ruths, J. J. de Pablo, and M. Tirrell, “Multivalent ions induce lateral structural inhomogeneities in polyelectrolyte brushes,” *Science Advances* **3**, eaao1497 (2017).
- ⁴⁶D. Bracha and R. H. Bar-Ziv, “Dendritic and nanowire assemblies of condensed DNA polymer brushes,” *J. Am. Chem. Soc.* **136**, 4945–4953 (2014).
- ⁴⁷F. S. Csajka and C. Seidel, “Strongly charged polyelectrolyte brushes: A molecular dynamics study,” *Macromolecules* **33**, 2728–2739 (2000).
- ⁴⁸P. S. Crozier and M. J. Stevens, “Simulations of single grafted polyelectrolyte chains: ssDNA and dsDNA,” *J. Chem. Phys.* **118**, 3855–3860 (2003).
- ⁴⁹V. S. Guptha and P.-Y. Hsiao, “Polyelectrolyte brushes in monovalent and multivalent salt solutions,” *Polymer* **55**, 2900 – 2912 (2014).
- ⁵⁰P. Benetatos, E. M. Terentjev, and A. Zippelius, “Bundling in brushes of directed and semiflexible polymers,” *Phys. Rev. E* **88**, 042601 (2013).
- ⁵¹L. M. Sander, “Fractal growth processes,” *Nature* **322**, 789–793 (1986).
- ⁵²J. R. Nicolás-Carlock, J. L. Carrillo-Estrada, and V. Dossetti, “Fractality à la carte: a general particle aggregation model,” *Sci. Rep.* **6**, 19505 (2016).
- ⁵³J. R. Nicolás-Carlock, J. L. Carrillo-Estrada, and V. Dossetti, “Universal fractality of morphological transitions in stochastic growth processes,” *Sci. Rep.* **7**, 3523 (2017).
- ⁵⁴D. Frenkel and R. Eppenga, “Evidence for algebraic orientational order in a two-dimensional hard-core nematic,” *Phys. Rev. A* **31**, 1776–1787 (1985).
- ⁵⁵M. A. Bates and D. Frenkel, “Phase behavior of two-dimensional hard rod fluids,” *J. Chem. Phys.* **112**, 10034–10041 (2000).
- ⁵⁶B. Y. Ha and A. J. Liu, “Kinetics of bundle growth in DNA condensation,” *EPL (Europhysics Letters)* **46**, 624–630 (1999).
- ⁵⁷T. A. Witten and L. M. Sander, “Diffusion-limited aggregation, a kinetic critical phenomenon,” *Phys. Rev. Lett.* **47**, 1400–1403 (1981).
- ⁵⁸M. Tokuyama and K. Kawasaki, “Fractal dimensions for diffusion-limited aggregation,” *Phys. Lett. A* **100**, 337 – 340 (1984).
- ⁵⁹M. Matsushita, K. Honda, H. Toyoki, Y. Hayakawa, and H. Kondo, “Generalization and the fractal dimensionality of diffusion-limited aggregation,” *J. Phys. Soc. Japan* **55**, 2618–2626 (1986).
- ⁶⁰T. Mima, T. Kinjo, S. Yamakawa, and R. Asahi, “Study of the conformation of polyelectrolyte aggregates using coarse-grained molecular dynamics simulations,” *Soft Matter* **13**, 5991–5999 (2017).
- ⁶¹J. D. Honeycutt and D. Thirumalai, “The nature of folded states of globular proteins,” *Biopolymers* **32**, 695–709 (1992).
- ⁶²H. J. Limbach, A. Arnold, B. A. Mann, and C. Holm, “ESPReso – an extensible simulation package for research on soft matter systems,” *Comput. Phys. Commun.* **174**, 704–727 (2006).
- ⁶³A. Arnold, O. Lenz, S. Kesselheim, R. Weeber, F. Fahrenberger, D. Roehm, P. Košovan, and C. Holm, “ESPReso 3.1 – Molecular Dynamics Software for Coarse-Grained Models,” in *Meshfree Methods for Partial Differential Equations VI*, Lecture Notes in Computational Science and Engineering, Vol. 89, edited by M. Griebel and M. A. Schweitzer (Springer, 2013) pp. 1–23.

Appendix A: Supplementary Figures

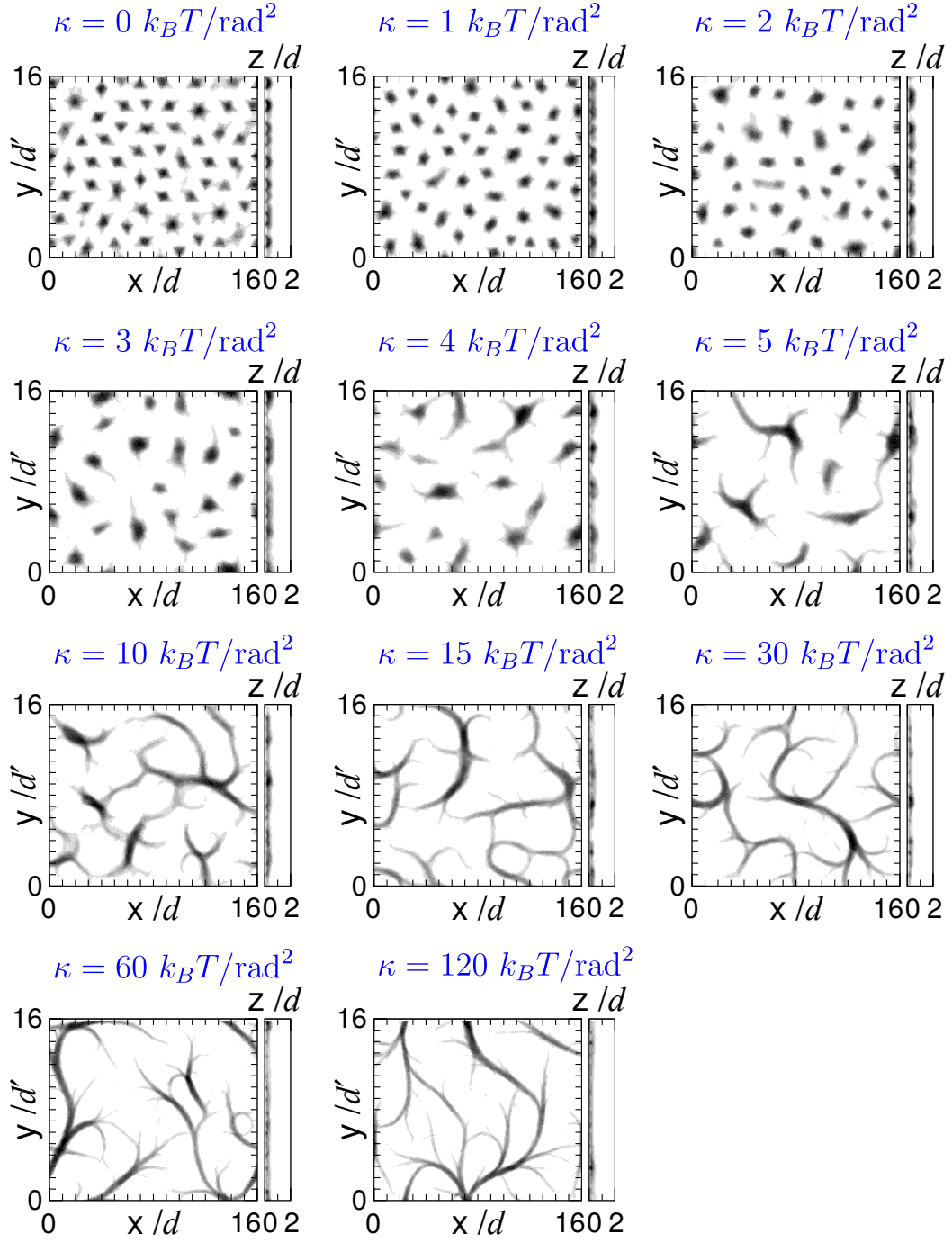


FIG. S1. Monomer density heatmap of PE brush averaged over time, $\langle \rho(x, y) \rangle$ and $\langle \rho(y, z) \rangle$, with various chain stiffness κ . The length unit d ($= 16a$) is the inter-chain distance at the grafting surface, and $d' = \sqrt{3}d/2$ on the y -axis.

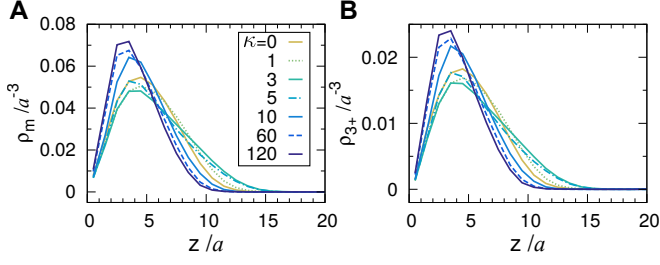


FIG. S2. Distribution of (A) chain monomers and (B) trivalent cations (3+) along z -axis for the brush chain with different κ .

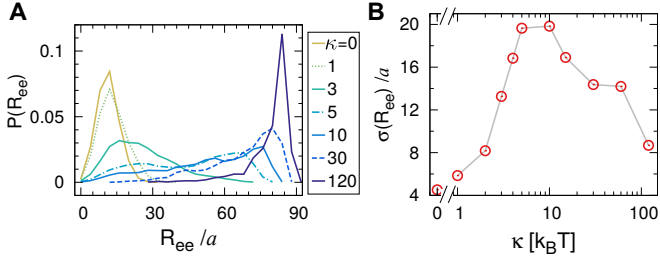


FIG. S3. (A) Probability density of the end-to-end distance (R_{ee}) of chains in the brush condensate. (B) Standard deviation of the R_{ee} of brush chains as a function of κ .

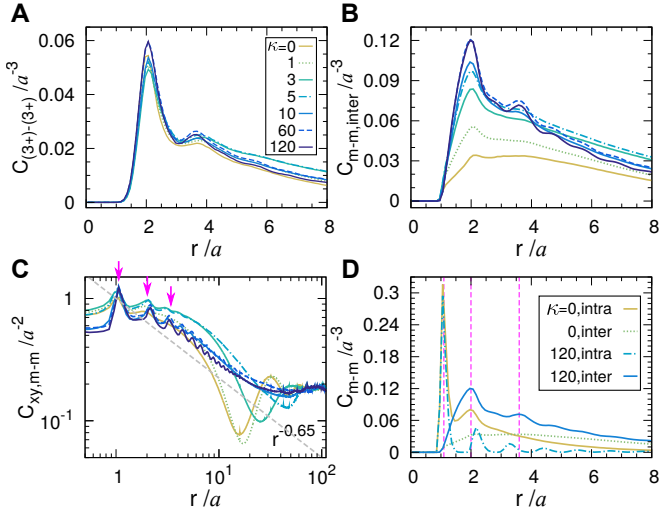


FIG. S4. (A) 3D radial distribution function between trivalent ions $C_{(3+)-(3+)}$, and (B) between monomers from different chains $C_{m-m,inter}$ at different κ . (C) 2D radial distribution function $C_{xy,m-m}$ between chain monomers at different κ shown in a log-log scale. The gray dashed line indicates a scaling relation of $C(r) \sim r^{-0.65}$. (D) 3D radial distribution function C_{m-m} between either intra-chain or inter-chain monomers at $\kappa = 0, 120 \text{ k}_B T/\text{rad}^2$. The arrows in (C) and vertical dashed lines in (D) label the length scales $r_{1,2,3}^*$ at which intermediate scattering function were calculated.

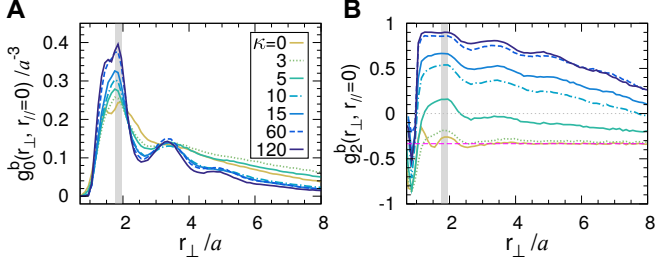


FIG. S5. Inter-chain bond ordering. (A) $g_0^b(r_\perp, r_\parallel = 0)$, and (B) $g_2^b(r_\perp, r_\parallel = 0)$ as a function of r_\perp with different κ , where the gray solid bar indicates the positions of the highest peaks.

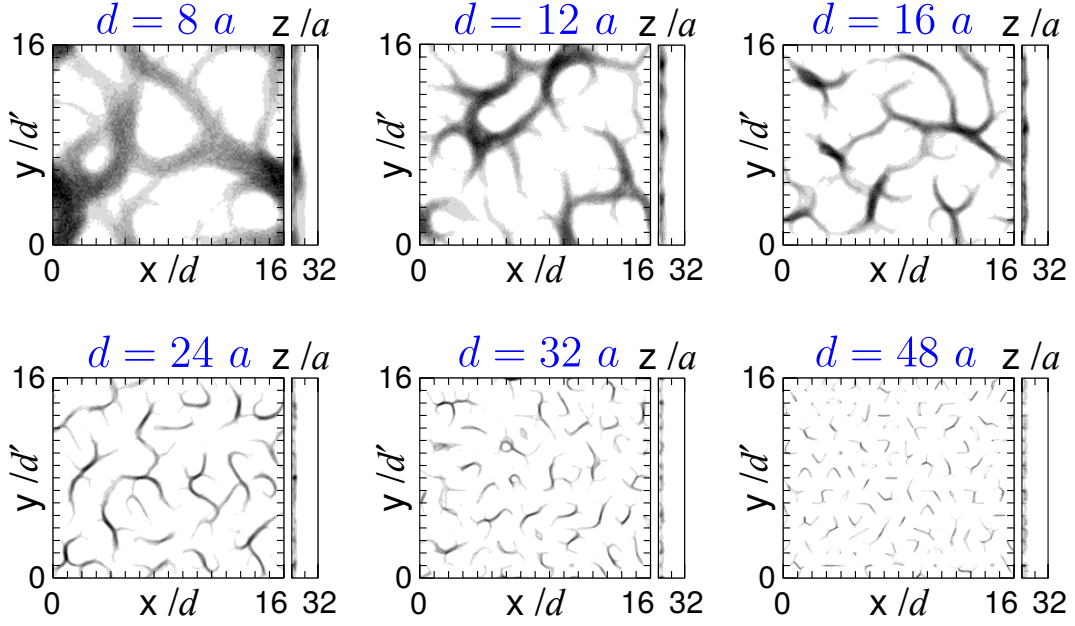


FIG. S6. Time-averaged monomer density heatmap of PE brush $\langle \rho(x, y) \rangle$ and $\langle \rho(y, z) \rangle$, at $\kappa = 10 k_B T / \text{rad}^2$, with different inter-chain spacing d on the grafting surface (i.e., with different grafting densities). The x - and y -axes in each plot are scaled with d and $d' = \sqrt{3}d/2$, respectively.

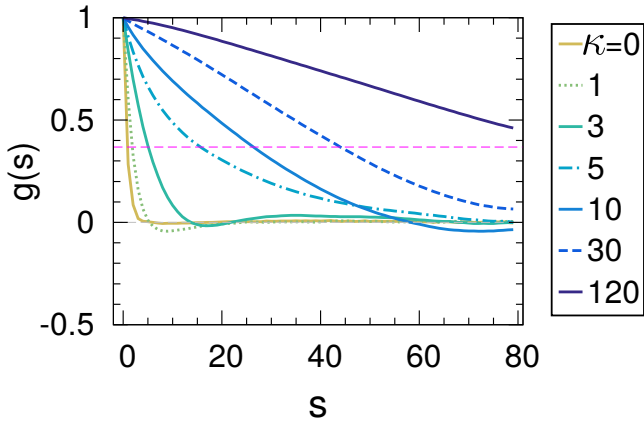


FIG. S7. Bond orientation correlation of chains in the brush, defined as $g(s) = \sum_i^{N-s} \vec{u}_i \cdot \vec{u}_{i+s} / (N-s)$, with a dashed magenta line indicating $g(l_p) = 1/e$.